

## Preliminary validation of the GLI cryosphere algorithms with MODIS daytime data

Masahiro Hori<sup>1</sup>, Teruo Aoki<sup>2</sup>, Knut Stamnes<sup>3</sup>, Bingquan Chen<sup>3</sup> and Wei Li<sup>3</sup>

<sup>1</sup>*National Space Development Agency of Japan, 1-8-10, Harumi, Chuo-ku, Tokyo 104-6023*

<sup>2</sup>*Meteorological Research Institute, 1-1, Nagamine, Tsukuba 305-0052*

<sup>3</sup>*Stevens Institute of Technology, Castle Point on Hudson, Hoboken, NJ 07030, U.S.A.*

**Abstract:** Preliminary validation of the two GLI cryosphere algorithms is conducted by applying them to MODIS daytime data on June 18, 2000. One of the algorithms has been developed for the discrimination of cloud/clear and snow/sea-ice, and the other for the retrievals of snow grain size and mass fraction of impurities mixed in snow. Analysis results show that cloudy areas around the northern polar region are successfully discriminated from areas under clear condition with various surface types such as snow, open ocean and bare land. Reasonable spatial distributions of snow grain size and mass fraction of impurities around the North Pole are also successfully retrieved in the range from nearly 0.0 to over 5000  $\mu\text{m}$  for snow grain size and 0.0–0.2 ppmw for snow impurities. Finally, possible sources of error in the retrieved parameters and remaining development points on the present version of the GLI algorithms to be improved for future advances are discussed.

### 1. Introduction

Snow and ice cover in the cryosphere, which is characterized by high reflectance in the shortwave radiation region and high emissivity in the longwave radiation domain and also by its large water volume, is an important target to be monitored from space in order to study the earth-atmosphere radiation budget in climate study and to estimate water resources in hydrological study.

Among various geophysical parameters in the cryosphere the extents of snow and ice cover on the earth are primary parameters to be monitored from space for those studies. Snow cover extent over Northern Hemisphere lands has been measured by the National Oceanic and Atmospheric Administration (NOAA) since 1966 with polar-orbiting visible satellites (Matson, 1991). Passive microwave sensors such as Nimbus/SMMR and SSM/I onboard DMSP have also provided information to determine snow and ice cover extents since 1978 (Chang *et al.*, 1990; Cavalieri *et al.*, 1984; Robinson *et al.*, 1993). Monitoring with TERRA/MODIS has just started in 2000 (Hall *et al.*, 1995).

Snow grain size and mass fraction of impurities mixed in snow, which have never been monitored from space operationally so far, can also be important targets, because snow grain size and mass fraction of impurities are closely related to the spectral albedos of the snow surface in the near infrared and the visible wavelength regions, respectively

(Warren, 1982). Thus, monitoring the spatial and temporal distributions of those snow parameters from space can provide useful information on the radiation budget, the amount of melting water and snow lifetime (Warren and Clarke, 1986).

Past studies of snow grain size and snow impurities have accumulated theoretical and practical knowledge on the retrieval of those snow parameters from space. Warren and Wiscombe (1980) and Wiscombe and Warren (1980), who conducted simulation studies on the spectral albedo of a snow surface, reveal that the spectral albedo strongly depends on the mass fraction of impurities in the visible wavelength region and also on snow grain size in the near infrared region. The larger the mass fraction of impurities and snow grain size are, the lower the albedos in the visible and the near infrared regions are, respectively. Fily *et al.* (1997) succeeded in the retrieval of snow grain size, which is close to the grain size obtained by field measurements at the snow surface in the Alps, using the near infrared channel (TM4: 0.76–0.90  $\mu\text{m}$ ) of Landsat TM. Aoki *et al.* (2000) conducted field observations of both the spectral albedo of snow surface and vertical profiles of various physical parameters in the snow layer, and also conducted simulation studies on the bi-directional reflection distribution function (BRDF) of the snow surface with the radiative transfer model. One of their findings is that the optically equivalent grain size giving the simulated snow albedo best matched to the observed albedo is close to the order of the branch width of dendrites for new snow or of the dimension of the narrower portion of broken crystals rather than the physical size of each snow crystal. In regard to snow impurities, their field measurement results suggest that snow impurities are concentrated at the snow surface by dry fallout of atmospheric aerosols. Comparing the simulated BRDF with the measured one reveals that a smooth phase function such as the Henyey-Greenstein (HG) phase function is more suitable to simulate the BRDF of a snow surface than one calculated from Mie scattering theory. In addition, their results show that the shorter the wavelength, the closer the BRDF of snow surface is to isotropic.

As stated above, monitoring both snow grain size and mass fraction of impurities operationally from space is an important task for climatic and hydrological earth science, and the necessary theoretical and technical bases have been established. The National Space Development Agency of Japan (NASDA) has been developing the multi-spectral radiometer called Global Imager (GLI) onboard the Advanced Earth Observing Satellite II (ADEOS-II) polar orbiter to be launched in 2002 (Nakajima *et al.*, 1998) and plans to make observations of various geophysical parameters on a global scale every 4 to 16 days. In cryosphere science fields snow and sea-ice cover extents and the spatial distributions of snow grain size and mass fraction of impurities are defined as geophysical parameters to be retrieved operationally with the GLI observations (Stamnes *et al.*, 1998, 1999). For the retrieval of those parameters, two algorithms have been developed. One is an algorithm for cloud/clear and snow/sea-ice discriminators over a snow surface (algorithm code: CTSK1) and the other is for the retrieval of snow grain size and mass fraction of impurities (CTSK2b1) (Stamnes, 1999a, b).

In this paper those two GLI cryosphere algorithms developed by Stamnes are tested using the data of the TERRA/MODIS sensor which was launched at the end of 1999, in order to validate the current performance of the GLI algorithms by comparing the

retrieved snow parameters with parameters measured in past studies or the spectral features of the observed fields of view, and to determine what further improvements are needed for the operational phase after the launch.

## 2. GLI algorithms

Snow and ice cover extents are determined for each pixel by the algorithm for cloud/clear and snow/sea-ice discriminators (CTSK1). CTSK1 first distinguishes clear pixels from cloudy pixels and then classifies the clear pixels into 6 types of surface elements such as “snow over land”, “snow over sea-ice”, “bare land”, “bare sea-ice”, “open ocean” and “cloud shadow”. The classified surface elements in 6 types and cloud confidences of 3 levels are expressed in the output 8 bit/pixel flag in binary form. On the other hand, snow grain size and mass fraction of impurities are generated as independent parameters from the algorithm for the retrieval of snow grain size and mass fraction of impurities (CTSK2b1). In both algorithms, radiances in the visible and the near infrared spectral bands are first converted to reflectances ( $R$ ) defined in the following equation,

$$R = \pi I / (F_0 \cos \theta_0), \quad (1)$$

where  $I$  is the calibrated radiance from Level-1B data (in this study MODIS level-1B MOD021KM are used.),  $F_0$  is the extraterrestrial solar irradiance (from Thekaekara (1974) in this study) without any consideration of channel filter response functions and  $\theta_0$  is solar zenith angle from geolocation data (MOD03). Radiances in the thermal infrared channels are converted to brightness temperatures using the Planck function. In this study, the appropriate MODIS channel in which center wavelength is the closest to that of the corresponding GLI channel is selected for testing the GLI algorithms. Selected channels are summarized in Table 1. The following sections outline the CTSK1 and CTSK2b1 algorithms.

### 2.1. Cloud/Clear and Snow/Sea-ice discriminators (CTSK1)

The algorithm developed by Stamnes (1999a) is used for cloud detection and surface classification within a given field of view (1 km at nadir). As shown in Table 1, reflectances and brightness temperatures of 10 channels in the range from the visible to the thermal infrared wavelength regions are used in threshold tests for cloud detection and surface classification. The algorithm first selects daytime or nighttime mode by checking the solar zenith angle for each field of view. Then the cloud detection and the surface classification tests defined in the selected mode are performed. In this study only MODIS daytime data are used as explained later (Section 3). Thus only tests in the daytime mode are described here.

The cloud detection test consists of two threshold tests, 1) brightness temperature difference test  $BT_{3.7} - BT_{11}$  and 2) reflectance test  $R_{1.38}$ , with minimum and maximum threshold values for each test. Each test returns a cloud confidence level between 0 and 1, where 1 represents high confidence in cloudy condition, and 0 represents clear condition. By comparing the test value with the minimum and maximum threshold values, the confidence level to be returned from each test is determined as follows. In

Table 1. ADEOS-II/GLI channels to be used in the GLI cryosphere algorithms for cloud/clear and snow/sea-ice discriminators (CTSK1) and the retrieval of snow grain size and mass fraction of impurities (CTSK2b1) and the corresponding TERRA/MODIS channels.

GLI ch.	MODIS ch.	CTSK1	CTSK2b1	Usages
GLI01: 0.380 $\mu\text{m}$	-	-	□	Selection of aerosol model
GLI05: 0.460 $\mu\text{m}$	MDS03: 0.469 $\mu\text{m}$	-	○	Retrieval of snow grain size and mass fraction of impurities, Selection of aerosol model
GLI08: 0.545 $\mu\text{m}$	MDS04: 0.555 $\mu\text{m}$	○	-	"Bare sea ice" & "Snow over sea ice" detection
GLI13: 0.678 $\mu\text{m}$	MDS01: 0.645 $\mu\text{m}$	○	-	"Cloud" and "Snow over land" detection in daytime mode, "Bare sea ice" & "Snow over sea ice" detection
GLI19: 0.865 $\mu\text{m}$	MDS02: 0.858 $\mu\text{m}$	○	○	Retrieval of snow grain size and mass fraction of impurities, "Bare sea ice" & "Snow over sea ice" detection
GLI24: 1.050 $\mu\text{m}$	MDS19: 1.240 $\mu\text{m}$	○	-	"Bare sea ice" & "Snow over sea ice" detection
GLI27: 1.380 $\mu\text{m}$	MDS26: 1.375 $\mu\text{m}$	○	-	"Cloud" detection in daytime mode
GLI28: 1.640 $\mu\text{m}$	MDS06: 1.640 $\mu\text{m}$	-	-	For comparison with the GLI cloud detection tests
GLI30: 3.715 $\mu\text{m}$	MDS20: 3.750 $\mu\text{m}$	○	-	"Cloud" detection in daytime & nighttime mode
GLI31: 6.700 $\mu\text{m}$	MDS06: 6.720 $\mu\text{m}$	●	-	"Cloud" detection in nighttime mode
GLI34: 8.600 $\mu\text{m}$	MDS29: 8.550 $\mu\text{m}$	●	-	"Cloud" detection in nighttime mode
GLI35: 10.800 $\mu\text{m}$	MDS31: 11.030 $\mu\text{m}$	○	-	"Cloud" and "Snow over land" detection in daytime & nighttime mode
GLI36: 12.000 $\mu\text{m}$	MDS32: 12.020 $\mu\text{m}$	●	-	"Cloud" detection in nighttime mode

Only the data of channels with symbol "○" are used in this study. In the operational phase after the launch of ADEOS-II satellite the channels with symbol "●" will be employed for the cloud detection test in nighttime mode and the channel with "□" will be employed to select the aerosol model for the atmospheric correction in the mid-latitude area. The channel MDS06 (1.64  $\mu\text{m}$ ) is used in this study for the comparison with the test values used in the cloud detection test in CTSK1 in order to evaluate the performance of the cloud detection test in the algorithm (Section 4.1).

case the test value is greater than the maximum threshold value, the confidence level is 1.0. In case the test value is less than the minimum threshold value, the confidence level becomes 0.0. When the test value is between the minimum and the maximum values, the confidence level is determined between 0.0 and 1.0 by linear interpolation. For the final decision on the cloud detection test to be used the higher confidence level among these two threshold tests ( $BT_{3.7}-BT_{11}$  and  $R_{1.38}$ ) is chosen. If the higher confidence level is 1.0, the pixel is identified as "high confidence cloudy (100%)". If the higher confidence level is in the range of 0.5–1.0 or 0.0–0.5, "middle confidence cloudy (50–100%)" or "low confidence cloudy (0–50%)" is assigned to the field of view, respectively. Finally if confidence levels of both threshold tests are 0.0, the pixel is identified as "clear" and the following surface classification test is then applied.

The surface classification test is defined for land and for ocean areas separately. By referring to the land/water map, either land or ocean mode is selected for each field of view. In both modes the existence of snow is examined. Furthermore, in land

Table 2. The GLI cloud and surface classification tests executed in this study and their threshold test values (daytime mode in CTSK1).

Tests		Detection targets	Thresholds in this study
Cloud detection	$BT_{3.7} - BT_{11}$	Clouds	12 (min), 18K (max)
	$R_{1.38}$	Thin cirrus clouds	9 (min), 11% (max)
Surface classification	$R_{0.865} / R_{0.678}$ ,		0.45
	Ocean	Sea ice / Snow or Open ocean	0.7
	$NDII = (R_{0.545} - R_{1.05}) / (R_{0.545} + R_{1.05})$		
	$R_{0.678}$	Snow / Open ocean	20%
	Land	Bare land / Snow	20%
	$BT_{11}$		274.15K

mode either bare land or cloud shadow is determined and in ocean mode either open ocean or bare sea-ice is determined. The surface classification process is the combination of several threshold tests as in the case of cloud detection and is summarized in Table 2 together with their threshold values adapted in this validation with MODIS data. The primary goal of this study on the surface classification is to detect only snow and sea-ice and thus discrimination between bare land and cloud shadow is not performed.

In general, the near infrared band around  $1.64\mu\text{m}$  is considered as the most useful band to discriminate cloud from snow because of the strong contrast of reflectance between cloud and snow (Warren, 1982). Both GLI and MODIS have the  $1.64\mu\text{m}$  channel and actually the MODIS cloud masking algorithm uses the  $1.64\mu\text{m}$  channel in the determination of snow/ice background (Ackerman *et al.*, 2000). However, in case of GLI the data of the  $1.64\mu\text{m}$  channel will not be able to be acquired at full resolution on a global scale in the operational phase due to the limitation of data transfer. The field of view of the  $1.64\mu\text{m}$  channel on the GLI sensor is 250m whereas that of other channels used in the GLI cryosphere algorithms is 1 km and thus volume size of the  $1.64\mu\text{m}$  channel data becomes larger than that of the 1 km resolution channel data. It is estimated that even acquiring only daytime land area data of all the 250m resolution channels takes about 3 months with the maximum availability of the data relay transport satellite to be launched in the near future (Horiyama, 1998). Therefore the GLI cryosphere algorithms have been developed on the assumption that only 1 km resolution channels are available at their full resolution. In this paper MODIS  $1.64\mu\text{m}$  channel data are used only for validation of the effectiveness of the GLI cloud detection scheme.

## 2.2. Retrieval of snow grain size and mass fraction of impurities (CTSK2b1)

The algorithm for the retrieval of snow grain size and mass fraction of impurities was also developed by Stamnes (1999b). Basically the algorithm uses reflectances at two channels for the retrieval. One is the channel in the visible wavelength of  $0.460\mu\text{m}$

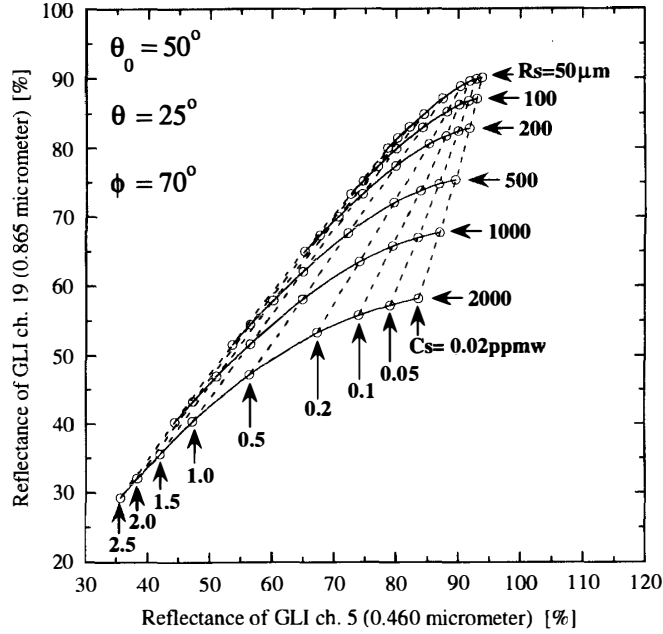


Fig. 1. Simulated reflectances at the top of the atmosphere in GLI ch. 5 ( $0.460\mu\text{m}$ ) and ch. 19 ( $0.865\mu\text{m}$ ) for various combinations of snow grain sizes ( $R_s$ ) and mass fractions of snow impurities ( $C_s$ ). Geometrical conditions are as follows: satellite zenith angle ( $\theta$ ) is  $25^\circ$ , solar zenith angle ( $\theta_0$ ) is  $50^\circ$  and relative azimuth angle ( $\phi$ ) is  $70^\circ$ . Simulated result for the case of “sub-arctic summer” as atmospheric model and “tropospheric aerosol” as aerosol model both adopted from MODTRAN is shown. It is assumed that snow grains are spherical and that snow impurities optically equivalent to carbon soot are mixed in snow as external mixture.

where the reflectance of snow is significantly related to mass fraction of impurities and the other is in the near infrared wavelength of  $0.865\mu\text{m}$  where the effect of snow grain size on snow albedo is more significant. For a given snow field of view by comparing the satellite observed reflectances in those two wavelengths with the simulated ones calculated as functions of various snow grain sizes (6 classes from  $50$  to  $2000\mu\text{m}$ ) and mass fractions of impurities (9 classes from  $0.02$  to  $2.5$  ppmw) with a bi-linear interpolation procedure, the final combination of both snow parameters which provide the reflectances closest to the observed ones is determined. The simulated reflectances are stored in lookup tables. One example of a combination between  $R_{0.460}$  and  $R_{0.865}$  stored in the lookup tables is indicated in Fig. 1, which is calculated with the atmospheric model of “sub-arctic summer” and the aerosol model of “tropospheric aerosol” in radiative transfer calculation as described later. The simulated reflectances are calculated with the radiative transfer model based on the DISORT multiple scattering algorithm (Stamnes *et al.*, 1988) which takes account of the BRDF of the snow surface. GLI channel filter response functions are also considered in the preparation of the lookup tables. Optical properties of snow used in the radiative transfer model are calculated based on Mie scattering theory which assumes spherical ice particles as snow grains. In the radiative transfer calculation one homogeneous snow layer with single combination of snow grain size and mass fraction of carbon soot mixed in the snow layer

as an external mixture is assumed. Thus, the retrieved snow grain size is not the physical size of crystals but optically equivalent spherical grain radius in  $\mu\text{m}$ , and the retrieved mass fraction of impurities is defined as the mass fraction of impurities optically equivalent to carbon soot in the unit of parts per million by weight (ppmw). For correction of the atmospheric effects on the reflectances at the top of the atmosphere, 9 lookup tables are prepared by considering the combinations of three different atmospheric models and seven different aerosol models included in the MODTRAN package. In particular, for the atmospheric correction in mid-latitude, the most appropriate aerosol model is selected by examining the reflectance difference  $R_{0.380} - R_{0.460}$  (Stamnes, 1999b). These model selection processes for the atmospheric correction will actually be performed in the operational phase. In this validation study, however, the input MODIS data are confined to data only around the northern polar region at latitude larger than about 50 degrees north in summer season and snow covered area is limited to the polar region. Therefore, for the correction of the atmospheric effect “sub-arctic summer” as atmospheric model and “tropospheric aerosol model” as aerosol model are directly selected among the prepared lookup tables. For the visible and near infrared channels used in the CTSK2b1 algorithm,  $0.469\mu\text{m}$  and  $0.858\mu\text{m}$  channels on MODIS are selected in this study (Table 1). The lookup tables prepared for the GLI channels are used without any modifications.

### 3. MODIS data processing

MODIS data are used for validation of the GLI algorithms, because the MODIS sensor is very similar to the GLI sensor in terms of the specification of channel wavelengths, the resolution of nadir field of view and orbit, so that MODIS data are the most appropriate for the performance test of the GLI algorithms. All spectral bands used in the GLI cryosphere algorithms except GLI ch. 1 ( $0.380\mu\text{m}$ ) and ch. 24 ( $1.05\mu\text{m}$ ) are available on the MODIS. For the GLI ch. 24, MODIS ch. 6 ( $1.24\mu\text{m}$ ) is used in this analysis alternatively (Table 1). The analysis target of the algorithm for the retrieval of snow grain size and mass fraction of impurities is the data of only daytime snow covered area, because reflectance data of visible channels are necessary to retrieve snow grain size and mass fraction of impurities. On the other hand, the algorithm for cloud/clear and snow/sea-ice discriminators can be applied to both daytime and nighttime data. To check the performance of both algorithms, particularly of the retrieval of snow grain size and mass fraction of impurities in wide areas around the polar regions, MODIS 1 day daytime data sets around the northern polar region on June 18, 2000, where solar zenith angles are larger than those in other seasons and thus all areas –even the North Pole area– are illuminated by solar radiation, are selected to be processed in this preliminary study.

MODIS Level-1B calibrated radiance data (product ID: MOD021KM) and geolocation data (MOD03) of about 30 scenes are used for this purpose. First, the observation data in each scene are gridded into a  $910 \times 910$  grid defined in a polar stereographic map projection with 10 km pixel dimensions at the North Pole by the nearest-neighbor resampling method. Second, the gridded images from all scenes are composited into one  $910 \times 910$  grid image. In the compositing process, if multiple



Fig. 2. RGB composite image of the  $910 \times 910$  grid image data around the northern polar region composed of 30 MODIS Level-1B scenes data on June 18, 2000. Red, Green and Blue channels are MDS01 ( $\lambda = 0.645 \mu\text{m}$ ), MDS04 ( $0.555 \mu\text{m}$ ) and MDS03 ( $0.469 \mu\text{m}$ ) in reflectance, respectively.

observation data from different orbits overlap on a grid cell, the earlier observation is selected as a single representative. The GLI algorithms are then applied to the composited grid image data. In Fig. 2 an RGB composite image of the  $910 \times 910$  grid image data is shown. MODIS ch. 1 ( $0.645 \mu\text{m}$ ), ch. 4 ( $0.555 \mu\text{m}$ ) and ch. 3 ( $0.469 \mu\text{m}$ ) in reflectance are assigned to Red, Green and Blue channels, respectively. Because of the specification of the narrower GLI scan angles ( $\pm 45^\circ$ , corresponding to 1600 km swath width) in contrast to the scan angles of MODIS ( $\pm 65^\circ$ , 2230 km), only the data within the scan angles of  $\pm 50^\circ$  in MODIS data are processed in the gridding process. Calibrated radiances of each channel stored in the Level-1B files are used without any additional corrections. Through the analysis of the wide area data around the North Pole the performance of the GLI cryosphere algorithms for the data of various surface elements, clouds and under various geographic conditions are examined. Unfortunately, truth data obtained by field observations are not available for validation of retrieved snow parameters in this study. Instead, the retrieved snow parameters are evaluated through comparison with values measured in past studies and with spectral features in the MODIS reflectance or brightness temperature data.



## 4. Results

### 4.1. Cloud/Clear and Snow/Sea-ice discriminators (CTSK1)

Figures 3a and 3b show the images of  $BT_{3.7}-BT_{11}$  and  $R_{1.375}$ , respectively, which are employed as the threshold test values in the cloud detection process in CTSK1. Fig. 3c shows the image of  $R_{1.64}$ . And Figs. 4a to 4c show histograms of the corresponding images in Figs. 3a to 3c. In Figs. 4a and 4b the minimum threshold values employed in determination of the cloud confidence level are indicated by vertical lines.

In general, satellite observed radiance in the  $3.7\mu\text{m}$  band in daytime data includes not only the component of thermal emission from a given field of view but also the large amount of solar radiation reflected at the ground surface or top of clouds while there is little solar radiation in  $11\mu\text{m}$  band, which makes  $BT_{3.7}$  larger than  $BT_{11}$  in case of a field of view with high reflectance in  $3.7\mu\text{m}$  ( $R_{3.7}$ ). Because  $R_{3.7}$  of clouds is generally higher than that of the snow surface, the brightness temperature difference  $BT_{3.7}-BT_{11}$  of clouds becomes larger than that of the snow surface and thus can be used as an effective discriminator between clouds and snow (Yamanouchi and Kawaguchi, 1992). In the histogram of  $BT_{3.7}-BT_{11}$  (Fig. 4a) apparent bimodal peak can be seen with the local minimum at around 15 K. The peak in the range of larger values ( $BT_{3.7}-BT_{11} > 15\text{ K}$ ) indicates cloud while that of lower values shows the feature of clear pixels such as snow. In this study the  $BT_{3.7}-BT_{11}$  value of 12 K, slightly lower than the local minimum, is employed as the minimum threshold value in the threshold test in order to minimize the misidentification of cloud pixels as snow.

Because of strong water vapor absorption around  $1.375\mu\text{m}$ , almost all of the upward radiation in the  $1.375\mu\text{m}$  spectral band reflected at the ground surface is absorbed in the atmosphere under clear condition and cannot reach the altitude of the satellite. But if there is a cloud layer in the atmosphere, the path length from the top of the cloud layer to the satellite is shorter than that from the ground; thus, the radiance reflected at the cloud top can be observed by satellite. The higher the cloud layer, the shorter the atmospheric path length. Thus  $R_{1.375}$  test can be used as an effective detection test of higher clouds such as cirrus clouds. However, in polar regions such as Antarctica and Greenland with a thick ice sheet over 3000 m in height, where the amount of water vapor in the atmosphere is generally less than that at lower latitude,  $R_{1.375}$  can be large enough to be observed by satellite even under clear sky condition as can be seen in the Greenland area in Fig. 3b. Thus, the minimum threshold value of  $R_{1.375}$  should be determined with the above consideration for those areas. In this study the minimum threshold value of 9% is employed (Fig. 4b) in order to not identify the top area of the ice sheet in Greenland as cloudy, where  $R_{1.64}$  is low enough to be identified as clear pixels (Fig. 4c). In case of the Antarctic ice sheet, a different threshold value of  $R_{1.375}$  might be necessary.

Comparing Figs. 3a ( $BT_{3.7}-BT_{11}$ ) and 3b ( $R_{1.375}$ ) indicates that the areas in the latter  $R_{1.375}$  image with the  $R_{1.375}$  values higher than the minimum threshold value almost overlap with those in the  $BT_{3.7}-BT_{11}$  image in this study. Comparing Fig. 3a ( $BT_{3.7}-BT_{11}$ ) with Fig. 3c ( $R_{1.64}$ ), where the latter is the effective discriminator between snow and clouds as stated before, indicates that the areas with lower  $R_{1.64}$  values in the Arctic Ocean and Greenland overlap well with those of  $BT_{3.7}-BT_{11}$ . This consistency verifies

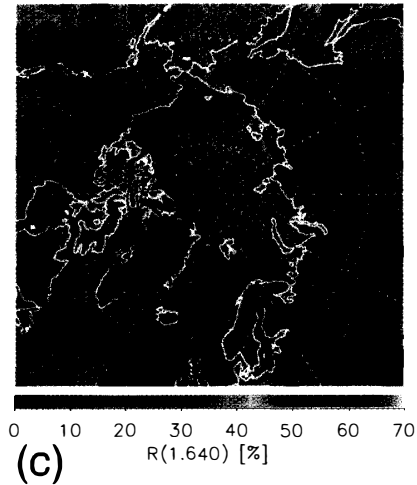
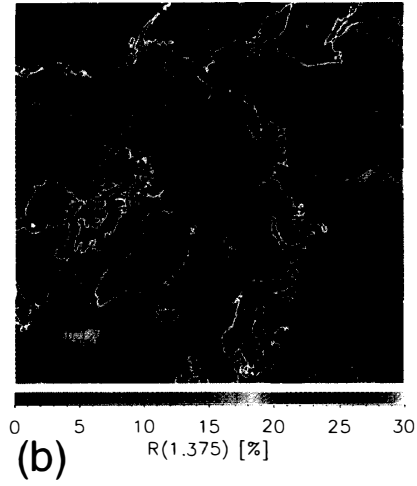
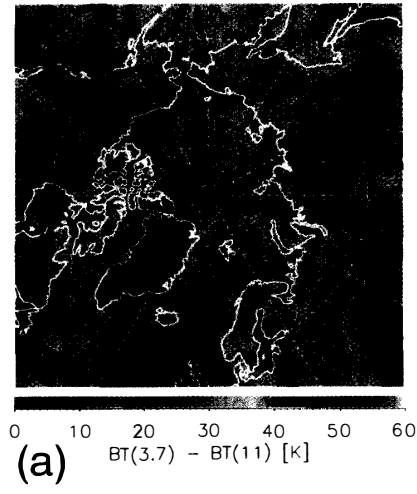


Fig. 3.

Fig. 3. Color-coded images of (a)  $BT_{3.7} - BT_{11}$ , (b)  $R_{1.375}$  and (c)  $R_{1.640}$  around the northern polar region.

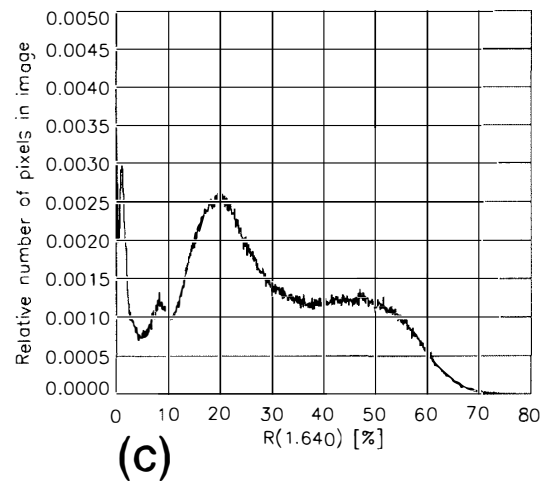
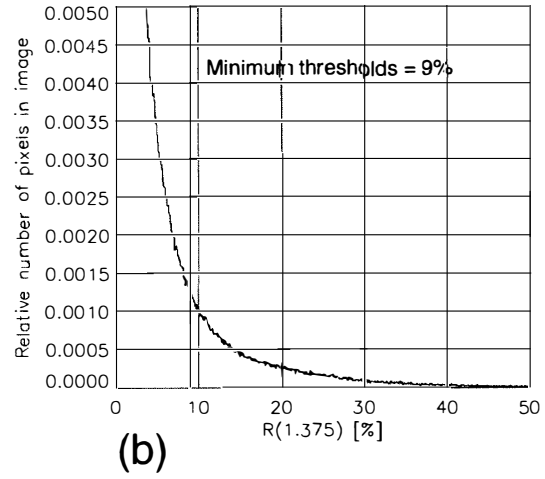
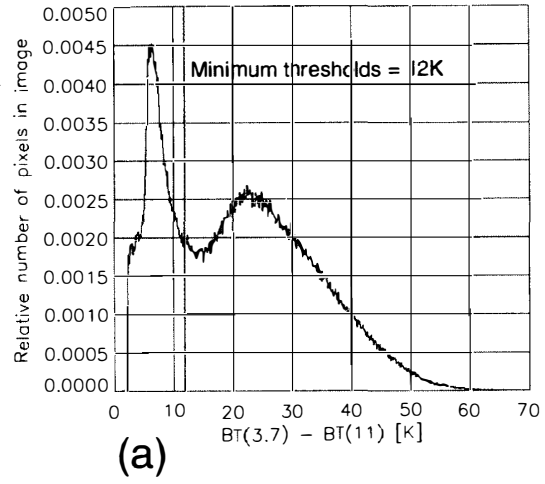


Fig. 4.

Fig. 4. Histograms of the corresponding data shown in the Figs. 3a-c, (a)  $BT_{3.7} - BT_{11}$ , (b)  $R_{1.375}$  and (c)  $R_{1.640}$ . The minimum threshold values of  $BT_{3.7} - BT_{11}$  and  $R_{1.375}$  adopted in this study are also indicated by vertical lines in (a) and (b).

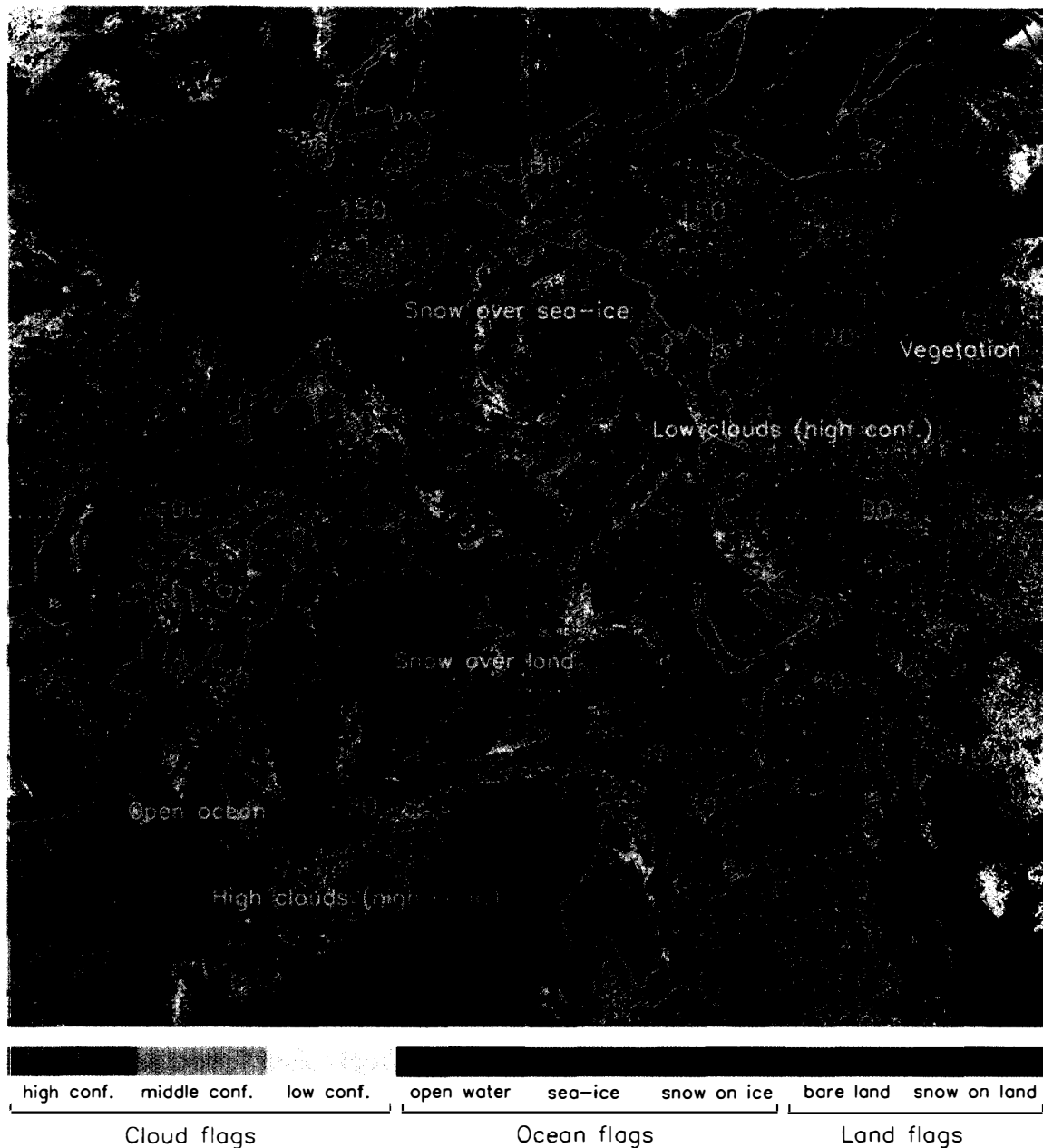


Fig. 5. Color-coded cloud and surface classification flag image generated with the GLI CTSK1 algorithm. The points shown by the red colored symbol “●” with surface or cloud type name are the pixel locations of which spectral features are shown in Fig. 6.

that the  $BT_{3.7}-BT_{11}$  test can be used as the effective snow/cloud discriminator comparable to the  $R_{1.64}$  test for the processing of northern polar region data.

Figure 5 shows a color-coded image of the 8bit/pixel output flag generated with the CTSK1 algorithm. Because the input data are from summer (June 18, 2000), there are few pixels identified as snow over land except the pixels in Greenland and northeastern Canada. Sea-ice with snow cover is mostly within the Arctic Ocean. As will be discussed later, snow over the sea-ice on the Arctic Ocean north of Alaska can be

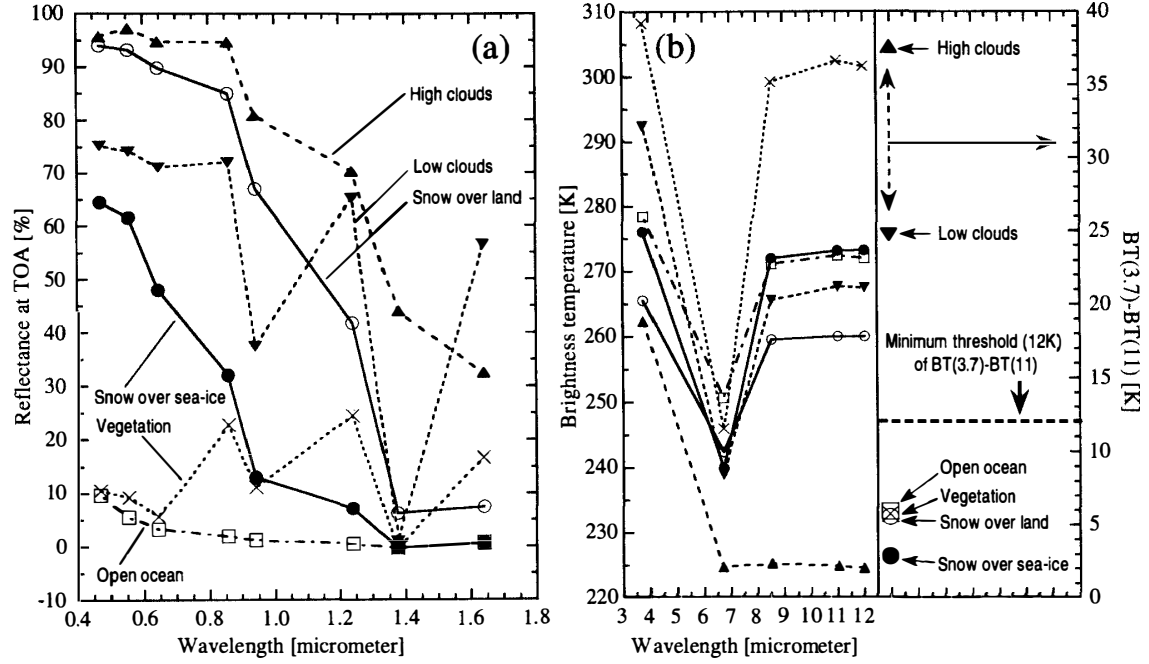


Fig. 6. (a) Reflectances at the top of the atmosphere of the 8 visible and near infrared channels obtained for the 6 pixels shown in Fig. 5. Types of surface or cloud are indicated with the symbol “▲” for high clouds, “▼” for low clouds, “□” for open ocean, “●” for snow over sea-ice, “○” for snow over land and “×” for vegetation (bare land). (b) Brightness temperatures of the 5 thermal infrared channels and the brightness temperature difference of  $BT_{3.7}-BT_{11}$  for the 6 pixels with the same symbol for each type as (a). In both figures viewing angle dependences of all channels data are not corrected.

considered to be melting or old snow near the melting point, while there are few pixels identified as bare sea ice.

Among various classified elements in Fig. 5, four surface elements, that is, “snow over land”, “snow over sea-ice”, “open ocean” and “bare land” (bare land can be specified here as “vegetation” surface from its spectral feature of the reflectances in Fig. 6a), and two cloud types, “high (altitude) clouds” and “low (altitude) clouds” both with high confidence level (the high or low in altitude of each clouds are decided with  $R_{1.375}$ ), are selected at the 6 pixel positions, which are indicated with the red colored symbol “●” in Fig. 5, and their spectral features of reflectances, brightness temperatures and one of the cloud detection test value  $BT_{3.7}-BT_{11}$  are plotted in Figs. 6a and 6b. Each spectral line in Figs. 6a and 6b is obtained from one pixel at each selected position in Fig. 5. Reflectances are calculated with eq. (1) and brightness temperatures are calculated from radiances in each spectral band using the Planck function without correction for viewing angle dependence, as described in Section 2.

Although reflectances of all elements except that of high clouds become lower in the absorption bands such as 0.940 and 1.375  $\mu\text{m}$  in Fig. 6a, in other non-absorption bands the characteristic features of individual surface elements can be seen as follows: high albedo in the visible wavelength region of snow over land (Greenland) with the decrease

of albedo in the longer wavelength region to around  $1.64\mu\text{m}$  (Warren, 1982), steep increase of the albedo of bare land at around  $0.7\mu\text{m}$  wavelength which is characteristic of vegetation (Saito and Yamazaki, 1999) and high brightness temperatures over 300 K in the atmospheric window region around  $11\text{--}12\mu\text{m}$  characteristic of the inland area in daytime, and very low visible albedo less than 10% over the open ocean.

For high clouds, the reflectances are the highest at all wavelengths, even in the absorption bands, except at  $1.64\mu\text{m}$ ; and the brightness temperatures are the lowest among the 6 elements, reflecting the thick optical thickness and the low temperature of the high cloud top layer. Only at  $1.64\mu\text{m}$  the reflectance of low clouds exceeds that of high clouds as shown in Fig. 6a, which is partly due to the phase difference of cloud particles between solid (ice) and liquid (water) accompanied with the size difference of the cloud particles, as discussed by Warren (1982) for the comparison between cumulus and cirrus clouds. As for the spectral features of low clouds, comparison with the reflectances of snow over sea-ice is conducted here, because the low clouds in Fig. 5 are at high latitude ( $80^\circ\text{N}$ ) within the Arctic Ocean, thus the surface below low clouds is expected to be snow over sea-ice with albedo less than 65% in the visible region as shown in Fig. 6a. In the visible region low clouds simply raise the albedo of snow over sea-ice under clear condition to over 70%. In the near infrared region, except in the absorption bands, the difference in reflectances between low clouds and snow over sea-ice becomes larger, as the wavelength increases. This is because in the near infrared region the reflectances are strongly dependent on the particle radius of clouds and snow and the dependence becomes large with wavelength (Warren, 1982). Thus the large reflectance difference in the near infrared region actually reflects the difference in particle size between clouds and snow. As briefly stated in Section 2.1, this strong contrast of the reflectance in the near infrared region around  $1.64\mu\text{m}$  between clouds and snow is generally used for cloud/snow discrimination.

The reflectances of snow over sea-ice are always lower than those of snow over land in Fig. 6a, which can be caused mainly due to the difference of snow grain size.  $BT_{11}$  in Fig. 6b shows that the temperature of snow over sea-ice is nearly at the melting point (273.15 K) whereas that of snow over land is about 260 K. Therefore the snow over sea-ice can be under the condition of snow melting. Besides, the mixture of snow with different types of elements such as bare ice and open ocean surface within the field of view can also be considered as one cause of the lower reflectance of snow over sea-ice. As a result of the above causes, the reflectances of the snow over sea-ice in both visible ( $0.46\mu\text{m}$ ) and near infrared ( $0.86\mu\text{m}$ ) channels become lower far beyond the value ranges of the lookup table for the retrieval of snow grain size and mass fraction of impurities (Fig. 1). In such cases snow grain size and mass fraction of impurities are retrieved with extrapolation in the present version of the algorithms and thus possibly include large errors. The possibility of the sub-pixel mixture and its effects on the retrieval results, particularly on the retrieval of snow grain size and mass fraction of impurities, should be examined by using a high resolution satellite sensor.

Finally, in Fig. 6b  $BT_{3.7}-BT_{11}$  values of both high and low clouds become larger than the minimum threshold value of 12 K whereas those of surface elements are exclusively smaller than the threshold value. Therefore the good performance of the threshold test  $BT_{3.7}-BT_{11}$  for the cloud detection in CTSK1 can be confirmed also from

the spectral features of each element in Figs. 6a and 6b.

#### 4.2. Retrieval of snow grain size and mass fraction of impurities (CTSK2b1)

Figure 7 shows color-coded images of snow grain size (Fig. 7a) and mass fraction of impurities (Fig. 7b) from CTSK2b1 algorithms and that of brightness temperature  $BT_{11}$  (Fig. 7c). All parameter values are retrieved only for the snow pixels identified in Fig. 5. In Figs. 7a and 7b the retrieved values beyond the value ranges in the lookup tables, 50–2000  $\mu\text{m}$  for snow grain size and 0.02–2.5 ppmw for snow impurities, are determined by extrapolation as stated in the previous section. In this study, input data for the processing of the CTSK2b1 algorithm are the  $910 \times 910$  grid image data as shown in Fig. 2. In the grid data there are some distinct boundary lines resulting from multiple satellite data of different orbits, where geometric conditions such as satellite zenith angle and relative azimuth angles (relative difference between viewing azimuth angle and solar azimuth angle) change discontinuously from one side to the other across the line. For example, satellite zenith angle changes from around  $0^\circ$  to  $50^\circ$  and relative azimuth angle changes from about  $80^\circ$  to  $115^\circ$  at the boundary lines around the Arctic Ocean, north of Alaska, the Queen Elizabeth Islands and Greenland (not shown in this paper). Nevertheless, the output images of snow grain size and mass fraction of impurities show that smooth spatial distributions of both snow parameters around the North Pole are successfully retrieved, with slight discontinuities around the central part of Greenland and the Arctic Ocean north of Alaska where either the value of snow grain size or mass fraction of impurities exceeds the range in the lookup tables. This shows that basically the effects of snow BRDF and atmosphere over snow surface on the satellite observed reflectances around the North Pole are corrected well in case the retrieved snow parameter values are within the value ranges of the lookup tables.

With regard to the spatial distribution of snow grain size in Fig. 7a a wide variety of snow types with different grain sizes, for example, “new snow” for 20–100  $\mu\text{m}$ , “fine-grained older snow” for 100–300  $\mu\text{m}$  and “old snow near the melting point” for 1000–1500  $\mu\text{m}$ , are distributed widely around the North Pole (the relations between snow types and snow grain sizes are from Wiscombe and Warren, 1980). Snow grain size retrieved from space in this study or by optical measurements at the ground surface is the size of an optically equivalent ice sphere and is close to the order of the branch width of dendrites for new snow or of a dimension of narrower portion of broken crystals rather than the physical size of each snow crystals (Aoki *et al.*, 2000). Characteristics of the retrieved spatial distribution of snow grain size are the following. Snow over the thick ice sheet in Greenland consists of much smaller grains than snow over lower altitude areas. This is because the temperature of the snow over the ice sheet is kept lower than that at other lower altitude areas even in summer ( $BT_{11}=260$  K of snow over land in Fig. 6). Figure 7c shows that the brightness temperatures of most areas on the Greenland ice sheet are less than 265 K; on the contrary, those of snow over sea-ice areas are over 272 K, close to the melting point. Thus small grains in the fresh condition of new snow just after falling cannot become larger rapidly and thus narrower portion of crystal can be kept small for a long time, whereas snow grains over sea-ice can be easily metamorphosed and grow larger because of the higher surface temperature. In Fig. 7a snow grains over sea-ice in the Arctic Ocean tend to become

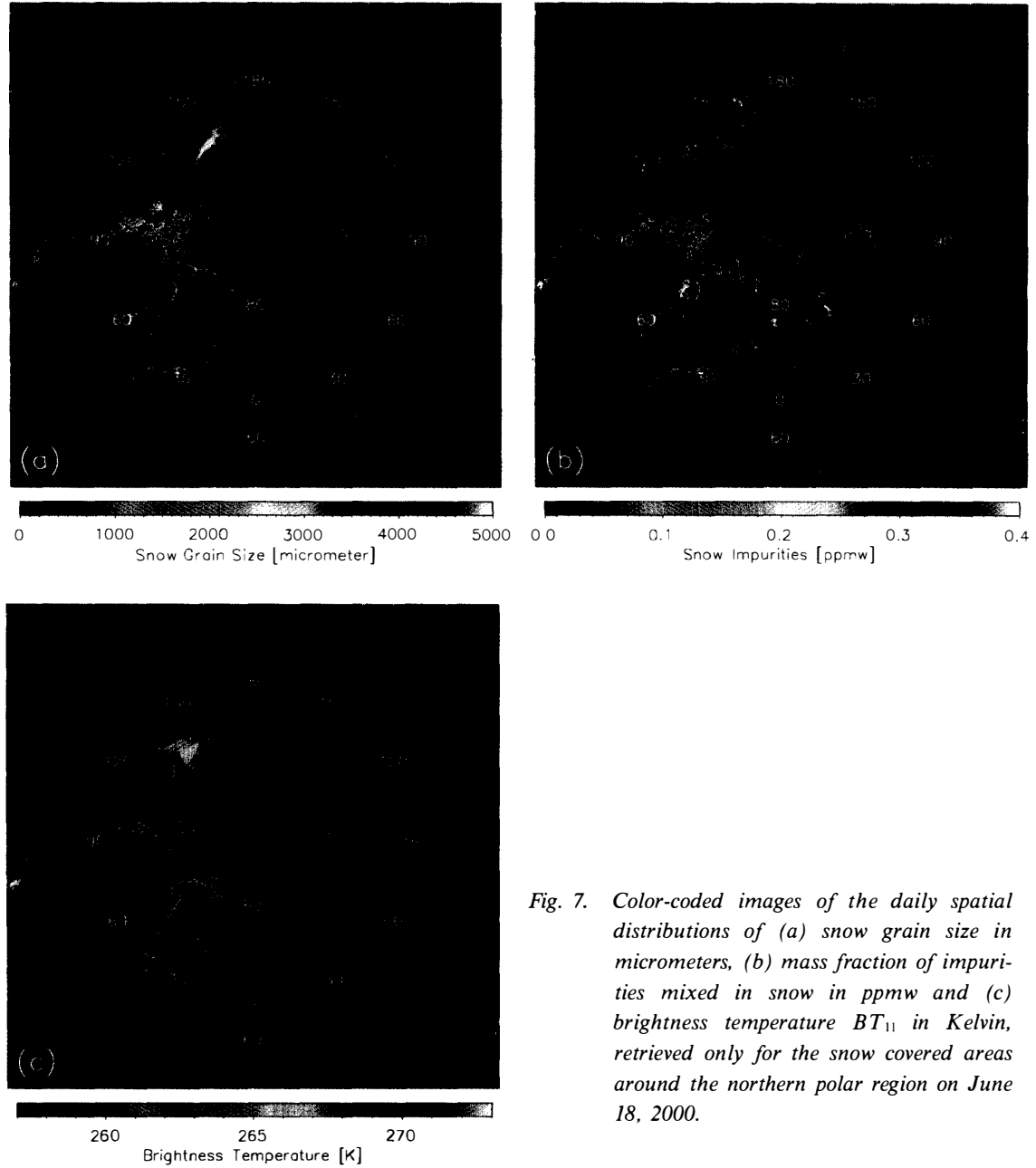


Fig. 7. Color-coded images of the daily spatial distributions of (a) snow grain size in micrometers, (b) mass fraction of impurities mixed in snow in ppmw and (c) brightness temperature  $BT_{11}$  in Kelvin, retrieved only for the snow covered areas around the northern polar region on June 18, 2000.

larger as latitude decreases, which is expected due to the spatial distribution of the time integrated solar energy received at the snow surface and that of air temperature. Upward heat flux from the ocean below sea-ice is also expected to be large enough to promote the melting of snow over sea-ice over a lower latitude ocean, where sea-ice concentration is expected to be lower and the sea-ice thickness is thinner than those at higher latitude. In this study, truth data of snow grain size observed at the snow surface on June 18, 2000 are not available. Instead, we investigated the relation between snow grain size and  $BT_{11}$ .  $BT_{11}$  is alternatively used as the snow surface temperature here. Although  $BT_{11}$  is not fully consistent with surface temperature ( $T_s$ )

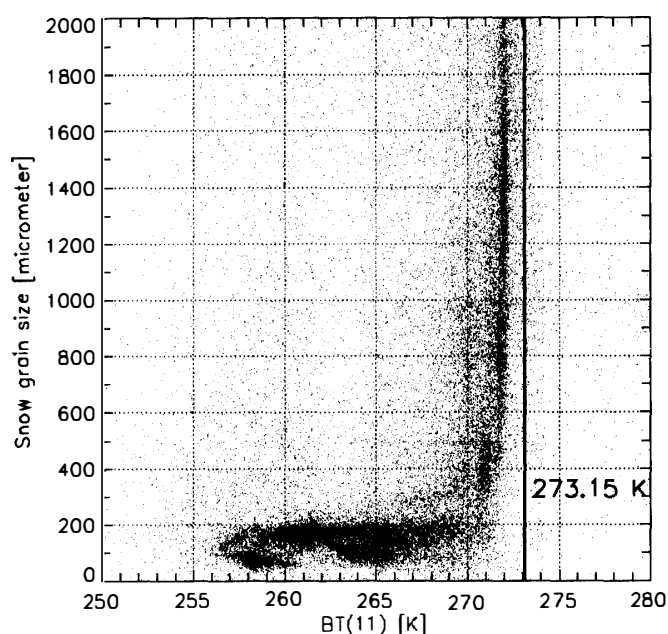


Fig. 8. Plot of  $BT_{11}$  in Kelvin versus snow grain size in micrometer. Thick vertical line indicates the melting point of ice at 1 atm (273.15 K).

due to the effect of water vapor absorption in the atmosphere, the simulation study with LOWTRAN by Yamanouchi *et al.* (1987) shows that  $BT_{11}$  of the snow surface around Syowa Station in Antarctica in summer is lower than  $T_s$  within a difference of 1–2 K. The same order of difference can be expected in this study.

Figure 8 shows a plot of  $BT_{11}$  vs. snow grain size. Most points in the low brightness temperature range below 270 K are distributed in the range of snow grain size less than  $300\mu\text{m}$  *i.e.* “fine-grained older snow”. Some scattered points are considered to be due to contamination by clouds and cloud shadow within those fields of view. At the brightness temperature of 272 K, which is nearly the same as the melting point, snow grain size steeply increases up to over  $2000\mu\text{m}$ . Actually in Figs. 7a and 7c steep changes of snow grain size and  $BT_{11}$  on slope areas near the coast in Greenland can be seen. This verifies that the spatial distribution of snow grain size in Fig. 7a reflects metamorphism and the growth of snow grains through sintering and melting processes depending on the surface temperature.

The spatial distribution of mass fraction of impurities in Fig. 7b, in which the retrieved values are less than 0.2 ppmw in most areas, reflects the reasonable contamination level of snow in a clean polar region. Pixels with large mass fractions over 0.4 ppmw can be seen in Bering Strait, Baffin Bay and around Svalbard, possibly due to sub-pixel contamination by open ocean or thin clouds by which visible reflectances within those fields of view are decreased. Because no truth data on June 18, 2000 are available, comparisons with past field observations are conducted here. Clarke and Noone (1985) collected snow samples at several locations around the sea-ice and continental areas in the northern polar region during winter and spring 1983, 1984. They measured the mass fraction of soot in the snow samples with an optical method. Their results show that the mass fraction of soot as the background level around the



northern polar region ranges from about 0.005 to 0.05 ppmw. Aoki *et al.* (1998) measured the spectral reflectances of snow surface at Barrow, Alaska in April, 1997 and found from comparison with simulation results that the measured reflectances of the snow surface are consistent with those of snow containing 0.1 ppmw carbon soot. The retrieved range for snow impurities from 0.0 to 0.2 ppmw without sub-pixel contamination in this study agrees well with those ranges reported in past observations, although the maximum value of this study (0.2 ppmw) is slightly larger than those of Clarke and Noone (0.05 ppmw) and Aoki *et al.* (0.1 ppmw). The wider range of this study can be considered due to the difference in season. In summer, the mass fraction of impurities in snow can be increased compared to winter or spring, because snowmelt in summer can concentrate insoluble impurities in the snow. Wind-blown dust from a non-snow covered area also contaminates the snow surface frequently in summer. The wider range can also be partly due to the actual change of the contamination level of snow cover around the northern polar region for the worse by anthropogenic aerosols such as Arctic Haze, and partly due to sub-pixel contamination by other surface elements. Roughness of snow surface can also be one of the causes, as will be mentioned in the next section.

## 5. Discussion

In this study the retrieved values of snow grain size and mass fraction of impurities in some regions vary beyond the value ranges stored in the lookup tables. In particular, snow grain size drastically changes from nearly 0 to over  $5000\mu\text{m}$  from area to area depending mainly on the surface temperature. For snow impurities, parameters are possibly beyond the ranges in the lookup tables in case of snow highly contaminated by anthropogenic aerosols in mid-latitude in winter. Therefore it will be necessary to validate the applicability of the lookup tables to the analysis of global data acquired in all seasons and also necessary to determine how to deal with pixels with values beyond the ranges of the lookup tables.

In this validation study the atmospheric correction for data around the northern polar region is performed with fixed atmospheric and aerosol models as described in Section 2.2. The atmospheric pressure and the concentration of aerosols, however, are not constant. Thus the reflectances in the two channels used in the retrieval of snow grain size and mass fraction of impurities must be affected by the temporal and spatial variations of the atmospheric constituent. In particular, because the effects of molecular and aerosol scattering are strong at shorter wavelengths, the reflectance of the visible channel is most likely affected rather than that of the near infrared channel. As Warren and Wiscombe (1980) mentioned, a mass fraction of soot mixed in snow has much more effect on the visible albedo of old melting large snow ( $r = 1000\mu\text{m}$ ) than on that of new small snow ( $r = 100\mu\text{m}$ ) (Fig. 7 of Warren and Wiscombe (1980)). In other words, an atmospheric correction error in the visible channel leads to a larger error in the retrieved value of snow impurities mixed in new snow than that in old melting snow. Therefore, the retrieved values of impurities in new snow around the area with high variability of aerosol concentration can be considered to include errors to a larger extent than other cases. The accuracy of atmospheric corrections for selected

atmospheric and aerosol models will need to be estimated in the future.

Sub-pixel level contamination in the snow pixels by other surface elements or clouds can decrease the accuracy of the retrieved snow parameters as described in the previous sections. In particular, in a forest area, snow cover can easily be masked by the forest canopy and cannot be observed from space, which increases the uncertainties in the retrieved snow cover extent in forest area (Hall *et al.*, 1995, 1998). The masking effect by forest cannot be examined in this study. It will be necessary to determine the reliability of the snow grain size and mass fraction of impurities retrieved from data which could be contaminated by vegetation, by interpreting the radiance as a function of vegetation density with vegetation indices (Saito and Yamazaki, 1999). It will also be effective to determine several confidence levels for snow and sea-ice elements similar to the cloud confidence level flags at the upper level in the snow parameter processing flow, by examining the possibility of contamination by other elements or clouds.

In this study, in the calculation of Mie scattering and radiative transfer for the preparation of the lookup tables, snow grains are assumed to be spherical ice grains existing in a homogeneous snow layer with a flat surface. According to Aoki *et al.* (2000), however, the snow BRDF observed in the real snow fields agrees well with the simulated BRDF calculated with the smooth HG phase function rather than that with the phase function from Mie scattering theory. Leroux *et al.* (1999) show that in the near infrared region the BRDF calculated with a hexagonal snow grain model is more consistent with their observed BRDF than that with a spherical grain model. In this way the spherical grain model, which is assumed in this study, has not been able to completely simulate the BRDF observed at the ground level. In addition, in the case of satellite remote sensing from space, the BRDF effect of the snow surface has to be taken into account together with the effects of the elevation and the slope of snow surface. Therefore, for more realistic simulation of snow reflectance in the radiative transfer calculation and for more precise retrieval of snow parameters from space, those effects have to be taken into account. To investigate these points, it will be necessary to analyze, for example, multiple observation data of the same location target with various observation times (*i.e.* solar zenith angles) and various viewing angles.

A snow surface is rarely perfect flat, although most studies including this study assume that it is. It can be considered that the radiance reflected at the snow surface with large roughness differs from the radiance coming from flat snow, because in the former case there can be glittering bright parts and dark shadow parts of the snow surface resulting from the roughness. In particular, in Antarctica there are a variety of snow surface types with and without roughness, such as sastrugi, snow dunes and glazed surface, etc. Therefore, the effect of the surface roughness together with that of the BRDF on the radiance coming from within each snow field of view will have to be investigated.

## 6. Conclusions

Snow and sea-ice cover extents and the spatial distributions of snow grain size and mass fraction of impurities around the northern polar region are successfully retrieved from MODIS data on June 18, 2000 using two GLI cryosphere algorithms. Compar-

isons of the retrieved snow grain size and mass fraction of impurities with the surface temperature expected from  $BT_{11}$  and past field observations of snow impurities, respectively, show that the retrieved ranges of both snow parameters are reasonable. These results show that the GLI algorithms, particularly the algorithm for the retrieval of snow grain size and mass fraction of impurities, can retrieve snow parameters from space satisfactorily, considering that these algorithms are the pre-launch versions. However, at the same time, many items in both algorithms still need to be investigated, for example: (1) the validity of the value ranges defined in the lookup tables in CTSK 2b1 for the processing of global and annual data; (2) the validity of the atmospheric and aerosol models considered in CTSK2b1 for correction of the atmospheric effect in various locations and seasons; (3) the effects of sub-pixel contamination by non-snow pixels such as clouds, forest and open ocean on the accuracy of the retrieved snow parameters with both CTSK1 and CTSK2b1; (4) the validity of the assumption of spherical snow grains and (5) the effect of assuming a flat surface of snow layer in CTSK 2b1 on the retrieval of snow parameters in real snow fields where snow grains are expected to be non-spherical grains such as hexagonal grains and the snow surface is usually rugged. It is necessary to conduct further validations of the GLI algorithms with MODIS and other high resolution satellite sensor data in the pre-launch phase in the coming year, in order to guarantee the quality of those GLI cryosphere products to be produced after the launch in 2002. There is also a plan to carry out field validation observations in Antarctica and Alaska with simultaneous satellite observations after the launch. After that, the snow parameters retrieved with guaranteed accuracy will be distributed in the operational phase by NASDA.

### Acknowledgments

This work was conducted as part of the ADEOS-II/GLI Cal/Val experiment supported by NASDA (National Space Development Agency of Japan). TERRA/MODIS data were provided by the GSFC Earth Sciences (GES) Distributed Active Archive Center (DAAC) at the NASA/Goddard Space Flight Center, Greenbelt, MD.

### References

- Ackerman, S.A., Strabala, K.I., Menzel, W.P., Frey, R.A., Moeller, C.C. and Gumley, L.E. (2000): Discriminating clear sky from clouds with MODIS. *J. Geophys. Res.*, **103**, 32141-32157.
- Aoki, Te., Aoki, Ta., Fukabori, M., Tachibana, Y., Zaizen, Y., Nishio, F. and Oishi, T. (1998): Spectral albedo observation on the snow field at Barrow, Alaska. *Polar Meteorol. Glaciol.*, **12**, 1-9.
- Aoki, Te., Aoki, Ta., Fukabori, M., Hachikubo, A., Tachibana, Y. and Nishio, F. (2000): Effects of snow physical parameters on spectral albedo and bidirectional reflectance of snow surface. *J. Geophys. Res.*, **105**, 10219-10236.
- Cavalieri, D.J., Gloersen, P. and Campbell, W.J. (1984): Determination of sea ice parameters with the Nimbus 7 SMMR. *J. Geophys. Res.*, **89**, 5355-5369.
- Chang, A.T.C., Foster, J.L. and Hall, D.K. (1990): Satellite sensor estimates of northern hemisphere snow volume. *Int. J. Remote Sensing*, **11**, 167-171.
- Clarke, A.D. and Noone, K.J. (1985): Soot in the arctic snowpack: a cause for perturbations in radiative transfer. *Atmos. Environ.*, **19**, 2045-2053.
- Fily, M., Bourdelles, B., Dedieu, J.P. and Sergeant, C. (1997): Comparison of *in situ* and Landsat Thematic

- Mapper derived snow grain characteristics in the Alps. *Remote Sensing Environ.*, **59**, 452–460.
- Hall, D.K., Riggs, G.A. and Salomonson, V.V. (1995): Development of methods for mapping global snow cover using moderate resolution imaging spectroradiometer data. *Remote Sensing Environ.*, **54**, 127–140.
- Hall, D.K., Foster, J.L., Verbyla, D.L., Klein, A.G. and Benson, C.S. (1998): Assessment of snow-cover mapping accuracy in a variety of vegetation-cover densities in central Alaska. *Remote Sensing Environ.*, **66**, 129–137.
- Horiyama, S. (1998): GLI data processing system. *Proceedings of the 3rd GLI Workshop*, 31–34.
- Leroux, C., Lenoble, J., Brogniez, G., Hovenier, J.W. and Dehaan, J.F. (1999): A model for the bidirectional polarized reflectance of snow. *J. Quant. Spectrosc. Radiat. Transfer*, **61**, 273–285.
- Matson, M. (1991): NOAA satellite snow cover data. *Palaeogeogr. Palaeoecol.*, **90**, 213–218.
- Nakajima, T.Y., Nakajima, T., Nakajima, M., Fukushima, H., Kuji, M., Uchiyama, A. and Kishino, M. (1998): Optimization of the advanced earth observing satellite II global imager channels by use of radiative transfer calculations. *Appl. Opt.*, **37**, 3149–3163.
- Robinson, D.A., Dewey, K.F. and Heim, R.R., Jr. (1993): Global snow cover monitoring: An update. *Bull. Am. Meteorol. Soc.*, **74**, 1689–1696.
- Saito, A. and Yamazaki, T. (1999): Characteristics of spectral reflectance for vegetation ground surfaces with snow-cover; Vegetation indices and snow indices. *J. Jpn. Soc. Hydrol. Water Resour.*, **12**, 28–38 (in Japanese with English abstract).
- Stamnes, K. (1999a): Cloud detection on snow/sea-ice (CTSK1). Algorithm description (draft). NASDA Internal Document, 3.4.1-1–3.4.1-28.
- Stamnes, K. (1999b): Snow grain size/impurities (CTSK2b1). Algorithm description (draft). NASDA Internal Document, 3.4.2-1–3.4.2-27.
- Stamnes, K., Tsay, S.-C., Wiscombe, W. and Jayaweera, K. (1988): Numerically stable algorithm for discrete-ordinate-method radiative transfer in multiple scattering and emitting layered media. *Appl. Opt.*, **27**, 2502–2509.
- Stamnes, K., Li, W., Xiong, X. and Chen, B. (1998): Remote sensing of cloud and surface properties in polar regions from GLI measurements on board ADEOS-II. *Proceedings of the 3rd GLI Workshop*, 220–225.
- Stamnes, K., Chen, B., Li, W. and Xiong, X. (1999): Cloud mask over snow/ice surface and snow grain size and impurity retrieval using ADEOS-II/GLI measurements. *Proceedings of ADEOS & ADEOS-II Joint Symposium/Workshop Vol. 1*, 3-31–3-39.
- Thekaekara, M.P. (1974): Extraterrestrial solar spectrum, 3000–6100 Å at 1-Å intervals. *Appl. Opt.*, **13**, 518–522.
- Warren, S.G. (1982): Optical properties of snow. *Rev. Geophys. Space Phys.*, **20**, 67–89.
- Warren, S.G. and Clarke, A.D. (1986): Soot from Arctic haze: Radiative effects on the Arctic snowpack. *Glaciol. Data*, **18**, 73–77.
- Warren, S.G. and Wiscombe, W.J. (1980): A model for the spectral albedo of snow. II: Snow containing atmosphere aerosols. *J. Atmos. Sci.*, **37**, 2734–2745.
- Wiscombe, W.J. and Warren, S.G. (1980): A model for the spectral albedo of snow. I: Pure snow. *J. Atmos. Sci.*, **37**, 2712–2733.
- Yamanouchi, T. and Kawaguchi, S. (1992): Cloud distribution in the Antarctic from AVHRR data and radiation measurements at the surface. *Int. J. Remote Sensing*, **13**, 111–127.
- Yamanouchi, T., Suzuki, K. and Kawaguchi, S. (1987): Detection of clouds in Antarctica from infrared multispectral data of AVHRR. *J. Meteorol. Soc. Jpn.*, **65**, 949–962.

*(Received February 5, 2001; Revised manuscript accepted June 21, 2001)*